The Astrophysical Journal Letters, 979:L41 (10pp), 2025 February 1 https://doi.org/10.3847/2041-8213/adabc2

Structure Functions of Rotation Measures Revealing the Origin of Fast Radio Bursts

Rui-Nan Li[1], Zhen-Yin Zhao[1], Qin Wu[1], Shuang-Xi Yi[2], and Fa-Yin Wang[1,3]
[1] School of Astronomy and Space Science, Nanjing University, Nanjing, 210023,People's Republic of China; fayinwang@nju.edu.cn
[2] School of Physics and Physical Engineering, Qufu Normal University, Qufu 273165, People's Republic of China
[3] Key Laboratory of Modern Astronomy and Astrophysics (Nanjing University) Ministry of Education, People's Republic of China
Received 2024 November 28; revised 2025 January 12; accepted 2025 January 14; published 2025 January 29

Abstract

Structure function (SF) analysis is a powerful tool for studying plasma turbulence. Theoretically, the SF of Faraday rotation measure (RM) is expected to include a geometric component due to the relative orientation of sight lines through an ordered magnetic field. However, observational evidence for this component remains elusive. Here, we report that the SFs of the binary PSR B1744–24A and the repeating fast radio burst (FRB) 20201124A exhibit both a periodic geometric component, caused by binary orbital motion, and a flat statistical component. The statistical component, induced by stochastic fluctuations in electron density and magnetic field, aligns with RM scatter derived from pulse depolarization. These findings indicate that FRB 20201124A has a binary origin and suggest that the periodic geometric component can serve as a diagnostic tool to identify binary companions.

Unified Astronomy Thesaurus concepts: Radio transient sources (2008); Magnetic fields (994); Interstellar medium (847); Radio bursts (1339)

1. Introduction

Fast radio bursts (FRBs) are luminous (D. R. Lorimer et al. 2007), millisecond-duration radio flashes originating from extragalactic sources with unknown physical origins (J. M. Cordes & S. Chatterjee 2019; B. Zhang 2023; Q. Wu & F.-Y. Wang 2024). Currently, advancements in highly sensitive radio telescopes such as the Five-hundred-meter Aperture Spherical radio Telescope (FAST) and the Green Bank Telescope (GBT) have facilitated comprehensive polarization measurements for FRBs and pulsars. Notably, active repeaters like FRB 20201124A, FRB 20220912A, and the binary system PSR B1744–24A have been extensively observed for their polarization properties (H. Xu et al. 2022; D. Li et al. 2023; Y.-K. Zhang et al. 2023; Y. Feng et al. 2024). Some observations suggest that some repeating FRBs exhibit polarization behaviors similar to those of binary systems (F. Y. Wang et al. 2022; R. Anna-Thomas et al. 2023; D. Li et al. 2023; K.M. Rajwade & J. van den Eijnden 2023; Z. Y. Zhao et al. 2023), providing critical insights into the local environments of their sources.

The rotation measures (RMs) of repeating FRBs are particularly valuable as they allow tracking of temporal changes over periods ranging from short (R. Luo et al. 2020; G. H. Hilmarsson et al. 2021b) to long intervals (G. H. Hilmarsson et al. 2021a; H. Xu et al. 2022). Observations indicate that significant RM variations are a hallmark of repeating FRB sources (R. Mckinven et al. 2023a), suggesting the presence of dynamic magnetoionic environments. These environments may include the wind nebulae of young magnetars (B. Margalit & B. D. Metzger 2018; Y.-H. Yang & Z.-G. Dai 2019; Z. Y. Zhao & F. Y. Wang 2021), supernova remnants (SNRs; A. L. Piro 2016; Y.-P. Yang & B. Zhang 2017; A. L. Piro & B. M. Gaensler 2018; Z. Y. Zhao et al. 2021), the stellar wind and disks of companions (F. Y. Wang et al. 2022; R. Anna-Thomas et al. 2023; Z. Y. Zhao et al. 2023), active galactic nucleus disks (Z. Y. Zhao et al. 2024), or outflows from massive black holes (B. Zhang 2018; J. I. Katz 2020; R.-N. Li et al. 2023). Y.-P. Yang et al. (2023) have investigated some astrophysical processes that may cause RM variations of FRBs. Despite these expectations, direct evidence pinpointing the exact origins of these dynamic magnetized environments remains elusive.

Investigations of turbulence, which is prevalent in astrophysical plasmas (D. Biskamp 2003; B. G. Elmegreen & J. Scalo 2004), could be key to distinguishing these environments. Turbulence is known to occur in various settings, including the solar wind, the interstellar medium (ISM) and intergalactic medium (IGM), accretion disks, and SNRs, playing a pivotal role in numerous astrophysical processes. These include the amplification of cosmic magnetic fields (D. Ryu et al. 2008), star formation (C. F. McKee & E. C. Ostriker 2007), particle acceleration (B. Zhang & H. Yan 2011; A. Lazarian et al. 2020), and magnetic reconnection (R. Wang et al. 2023). Turbulence naturally causes fluctuations in density and magnetic fields, which in turn lead to variations in RMs. The analysis of RMs using the structure function (SF) is a crucial statistical method for studying turbulence (A. Kolmogorov 1941; J. H. Simonetti et al. 1984; J. H. Simonetti & J. M. Cordes 1986; A. H. Minter & S. R. Spangler 1996; A. W. Clegg et al. 1992; A. Lazarian & D. Pogosyan 2016; S. Xu & B. Zhang 2016). As a result, SF analysis is also a vital tool for probing the plasma environments surrounding FRBs.

In general, the SF of the RM consists of a statistical component and a geometric component (J. H. Simonetti et al. 1984; A. W. Clegg et al. 1992). The stochastic fluctuations in free electron density and magnetic field will induce the statistical component. At large spatial separations, the SF of a source traveling in an extended homogeneous medium with an ordered magnetic field will have a substantial geometric component (J. H. Simonetti et al. 1984; A. W. Clegg et al. 1992) due to the changes in the line of sight (LOS) relative to the magnetic field direction. In order to properly understand any observational results, we must distinguish between the

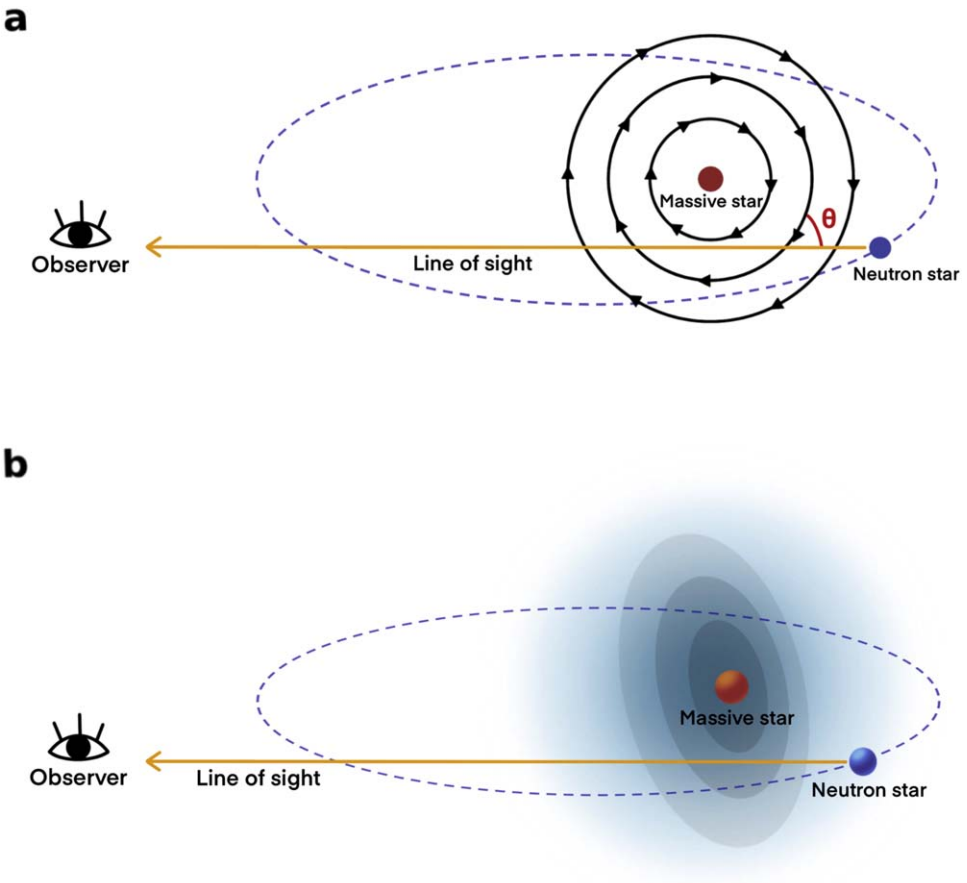

Figure 1. The schematic diagram of binary systems. Panel (a): the top-down view of binary systems. The black solid lines with arrows correspond to the toroidal magnetic field line in the decretion disk or winds. The yellow line is the LOS. The changes in the angle between the LOS and the magnetic field contribute to the geometric component in the RM SF. Panel (b): the 3D schematic diagram of binary systems. The gray shaded area indicates the decretion disk of the companion star. The blue shaded area indicates the stellar wind of the companion star.

statistical and geometric components. However, clear evidence of the geometric component has not yet been established from observations. In binary systems, the quasi-ordered magnetic field in the stellar wind or the decretion disk of the companion star could produce a geometric component in RM SFs, as shown in Figure 1. This geometric component will show periodic behavior due to the orbital motion. So, this characteristic feature can be used to examine the binary model for RM variations.

In this study, we aimed to investigate the properties of plasma turbulence near sources of FRBs by employing SF analysis. Additionally, we sought to determine the presence of the geometric component within the FRB and binary system. A detailed description of the data utilized for this analysis and an introductory overview are provided in Section 2. The results of SF analysis of RM and dispersion measure (DM) for the spider system PSR B1744–24A and seven active repeating FRBs are described in Section 3. A discussion and conclusions are presented in Section 4.

2. Data Sets and SF

2.1. Data Sets

The data sets used in SF analysis are summarized in Table 1. We use the bursts of FRB 20180916B with both RM and DM measurements by the Canadian Hydrogen Intensity Mapping Experiment (CHIME/FRB Collaboration et al 2019; R. Mckinven et al. 2023a; C. Ng et al. 2024), Low-Frequency Array (Z. Pleunis et al. 2021; A. Gopinath et al. 2024), and the upgraded Giant Metrewave Radio Telescope (S. Bethapudi et al. 2024). The RM and DM data of FRB 20201124A from FAST (Y. Feng et al. 2022; J.-C. Jiang et al. 2022; H. Xu et al. 2022) are used. FRB 20190520B has few bursts with RM and DM measurements (Y. Feng et al. 2022; C. H. Niu et al. 2022; R. Anna-Thomas et al. 2023). The number of DM data of FRB 20121102A is large. Meanwhile, the RM data are also adequate for analysis (L. G. Spitler et al. 2016; V. Gajjar et al. 2018; D. Michilli et al. 2018; G. H. Hilmarsson et al. 2021a; D. Li et al. 2021; D. M. Hewitt et al. 2022). There are a limited number of RM and DM data of FRB 20190303 for SF analysis (E. Fonseca et al. 2020; Y. Feng et al. 2022; R. Mckinven et al. 2023a; C. Ng et al. 2024). FRB 20220912A has more than 1000 bursts detected by FAST (Y.-K. Zhang et al. 2023; Y. Feng et al. 2024). We adopt the RM and DM data of PSR B1744–24A observed by GBT (D. Li et al. 2023).

2.2. SF

Considering an observational quantity $A(x)$, which is a function of position or time, x denotes the position on the plane of sky or the time of observation. The SF represents the mean-square difference between two observational quantities with spatial separation or temporal separation Δx. SF is defined as

$$D_{\rm A}(\Delta x) \equiv \langle [{\rm A}(x+\Delta x) - A(x)]^2 \rangle, \quad (1)$$

Table 1
The Data Used for SF Analysis

Source	Number of RM Observation	Number of DM Observation	References
PSR B1744–24A	625	596	D. Li et al. (2023)
FRB 20220912A	1204	1076	Y.-K. Zhang et al. (2023), Y. Feng et al. (2024)
FRB 20201124A	1679	811	H. Xu et al. (2022), J.-C. Jiang et al. (2022), Y. Feng et al. (2022), G. H. Hilmarsson et al. (2021b)
FRB 20190520B	16	207	R. Anna-Thomas et al. (2023), Y. Feng et al. (2022), C. H. Niu et al. (2022)
FRB 20190303A	17	55	R. Mckinven et al. (2023a), Y. Feng et al. (2022), E. Fonseca et al. (2020), C. Ng et al. (2024)
FRB 20180916B	74	54	R. Mckinven et al. (2023a), A. Gopinath et al. (2024), Z. Pleunis et al. (2021), CHIME/FRB Collaboration et al (2019), P. Chawla et al. (2020), C. Ng et al. (2024), S. Bethapudi et al. (2024)
FRB 20180301A	20	61	P. Kumar et al. (2023), R. Luo et al. (2020), Y. Feng et al. (2022)
FRB 20121102A	43	1724	L. G. Spitler et al. (2016), D. M. Hewitt et al. (2022), D. Michilli et al. (2018), G. H. Hilmarsson et al. (2021a), D. Li et al. (2021), V. Gajjar et al. (2018)

where $\langle ... \rangle$ represents an ensemble average. We neglect the distance along the LOS of different observational points. Based on the statistical descriptions (A. Lazarian & D. Pogosyan 2016), the power-law model of the SF is sufficient to capture the scaling properties of turbulence:

$$\widetilde{D}_A(\Delta x) = 2\sigma_A^2 \quad \frac{(\Delta x)^{m_A}}{l_A^{m_A} + (\Delta x)^{m_A}}, \tag{2}$$

where the variance of fluctuations is defined as

$$\sigma_A^2 = 0.81^2 \langle \delta(n_e B_\parallel)^2 \rangle \tag{3}$$

for RM density and

$$\sigma_A^2 = \langle \delta(n_e)^2 \rangle \tag{4}$$

for DM density. l_A is the correlation scale of density fluctuations, which distinguishes the energy dissipation scale and energy injection scale. Scales above the inner scale l_A of the shallow spectrum and scales below the outer scale l_A of the steep spectrum are considered as the inertial range where Equation (2) is applicable. m_A is the index of power-law functions. The index of SF can be used to determine whether the spectral index α, which depends on the turbulent spectrum, is shallow or steep (A. Lazarian & D. Pogosyan 2016):

$$\alpha = m_\phi - N, \quad \alpha > -3, \alpha = -m_\phi - N, \quad \alpha < -3, \tag{5}$$

where N is the dimensionality of turbulence in space. The theory of Kolmogorov turbulence was widely used in the research on the IGM and ISM. The Kolmogorov turbulence theory assumes the energy of large eddies was cascaded to the small eddies by kinetic-energy-conserving interactions where it was dissipated (B. G. Elmegreen & J. Scalo 2004). The Kolmogorov turbulence can be considered to be locally homogeneous and isotropic in the hydrodynamic case. MHD turbulence exhibits more complexity compared to the hydrodynamic case. In magnetohydrodynamics, the magnetic field establishes a preferred direction (D. Montgomery & L. Turner 1981; J. C. Higdon 1984; J. Cho & A. Lazarian 2002), leading to anisotropic statistical properties in the turbulence when it is affected by magnetization (A. Lazarian & E. T. Vishniac 1999; A. Lazarian & D. Pogosyan 2016). This kind of turbulence was found in different astrophysical environments. The statistical analysis reveals the presence of Kolmogorov spectra in Saturn's magnetosphere (S. B. Xu et al. 2023), Jupiter's magnetosheath (R. Bandyopadhyay et al. 2021), solar wind plasma (D. Shaikh & G. P. Zank 2010), star winds interacting with the ISM (M. Gallegos-Garcia et al. 2020), and the specific scale of the ISM (A. H. Minter & S. R. Spangler 1996; S. Xu & B. Zhang 2020).

The measurements of RM and DM provide us with unique information on the magnetized turbulence in the local environment. DM is defined as

$$\mathrm{DM} = \int_0^L n_e(l) dl, \tag{6}$$

where n_e is the number density of free electrons. The SFs of RM and DM depend on the power spectra $\mathcal{P}(k)$ of the fluctuations in $(n_e B_\parallel)(\boldsymbol{x})$ and $(n_e)(\boldsymbol{x})$, where k is the spatial wavenumber. Here we assume the power spectra of the RM and DM follow a power law with slope α (α being negative), i.e., $\mathcal{P}(k) \sim k^\alpha$. The screen can be thin when the correlation length of turbulent fluctuations exceeds the LOS extent of the Faraday screen: $\Delta R < l_{\mathrm{RM}}$. The SF of the RM can be expressed as (A. Lazarian & D. Pogosyan 2016; S. Xu & B. Zhang 2016)

$$D_{\mathrm{RM}}(\Delta x) \sim \begin{cases} \sigma_{\mathrm{RM}}^2 \Delta R \left(\dfrac{\Delta x}{l_{\mathrm{RM}}}\right)^{-(\alpha+2)}, & \Delta x < L \\ \sigma_{\mathrm{RM}}^2 \Delta R^2 \left(\dfrac{\Delta x}{l_{\mathrm{RM}}}\right)^{-(\alpha+3)}, & \Delta R < \Delta x < l_{\mathrm{RM}} \\ \sigma_{\mathrm{RM}}^2 \Delta R^2, & \Delta x > l_{\mathrm{RM}} \end{cases}. \tag{7}$$

For the above equations, $L \sim \Delta R$, $\sigma_{\mathrm{RM}} = \kappa^2 \langle \delta(n_e B_\parallel)^2 \rangle$ and $\sigma_{\mathrm{DM}} = \kappa^2 \langle \delta(n_e)^2 \rangle$. The SF of the DM is similar to the expressions above. It can be inferred that $D_{\mathrm{RM}}(\Delta x) \propto l^{-(\alpha+2)}$ or $D_{\mathrm{RM}}(\Delta x) \propto l^{-(\alpha+3)}$ in the inertial range and $D_{\mathrm{RM}}(l) \sim$ constant beyond the inertial range. Nevertheless, there is a limited effective range of the relation between the SF and power spectrum slope, and the slope of the power spectrum may be steeper than that in this range.

When we calculate the SFs of the RM and DM, each pair of RM and DM needs to be corrected by subtracting

Table 2
Power-law Relations for Turbulence Medium

Quantity		Exponent	
		3D	2D
2D, 3D power spectrum	$\mathcal{S}_2(q_s)$, $\mathcal{S}(q_s)$	$\alpha = -11/3$	$\alpha = -11/3$
SF	$D_\phi(d)$	$-(\alpha + 2) = 5/3$	$-(\alpha + 3) = 2/3$
Temporal SF	$D_\tau(\tau)$	$-(\alpha + 2) = 5/3$	$-(\alpha + 3) = 2/3$

Note. Power-law relations of temporal SF are only valid under proper motion assumption.

$(\sigma^2_{\rm RM}(x) + \sigma^2_{\rm RM}(x + \Delta x))$ and $(\sigma^2_{\rm DM}(x) + \sigma^2_{\rm DM}(x + \Delta x))$ to remove the noise bias caused by measurement uncertainties.

Three-dimensional (3D) Kolmogorov turbulence has a value of $\alpha = -11/3$ (A. Kolmogorov 1941), which corresponds to the steep spectrum, $D_{\rm RM}(l) \propto l^{5/3}$ or $D_{\rm RM}(l) \propto l^{2/3}$. When the transverse scale is much larger than the thickness of the observed Kolmogorov turbulent region, the power-law index is $2/3$, which reflects the behavior of 3D turbulence measured in a two-dimensional (2D) geometry. It is important to note that this is distinct from purely 2D turbulence, which exhibits an inverse cascade and different spectral properties. Table 2 summarizes the power-law relations for Kolmogorov turbulence including the 2D distribution of the fluctuating field. The temporal SF is converted from the spatial SF by assuming a constant velocity of the source.

3. Results

An SF measures the amount of fluctuations in a quantity as a function of the time of the fluctuations. The temporal RM SF can be described as (J. H. Simonetti et al. 1984; R. Mckinven et al. 2023a)

$$D_{\rm RM}(\Delta t) = \langle [{\rm RM}(t) - {\rm RM}(t + \Delta t)]^2 \rangle, \quad (8)$$

where the angle brackets denote an ensemble average over time separation Δt. RM is defined as

$${\rm RM} = 8.1 \times 10^5 \int_{\rm LOS} n_{\rm e} \boldsymbol{B} \cdot d\boldsymbol{l} \ {\rm rad\ m^{-2}}, \quad (9)$$

with the electron number density $n_{\rm e}$ (in units of ${\rm cm^{-3}}$), the magnetic field $\boldsymbol{B}$ (in units of G), and the distance l (in units of pc).

We first apply the SF analysis to the binary system PSR B1744–24A with uncommon polarization behaviors. The result is shown in panel (a) of Figure 2. The orange plus signs represent the measurements of $D_{\rm RM}$, and the blue points are the rebinned data. We can see that the SF of PSR B1744–24A shows a stochastic fluctuation and remains nearly constant for $\log(\Delta t) < -2$ days. For $\log(\Delta t) > -2$ days, it exhibits a trend that is similar to the trigonometric function and then enters into a decline phase, which is hard to explain by the turbulence theory (B. G. Elmegreen & J. Scalo 2004). The spatial SFs of the ISM (A. W. Clegg et al. 1992; A. H. Minter & S. R. Spangler 1996; M. Haverkorn et al. 2008), IGM (S. Xu & B. Zhang 2020; S. Xu et al. 2021), and SNRs (J. Shimoda et al. 2018; P. Saha et al. 2019) show rising power-law or flat form depending on the physical scale, instead of a decline phase as found in PSR B1744–24A. The RM variation has been interpreted as the orbital motion leading to the changes of the angle between the LOS and the magnetic field in the stellar wind (D. Li et al. 2023). We will try to explain it using the geometric component.

In a nearly homogeneous medium supported by the SF of DM, the geometric component caused by the change in $\boldsymbol{B} \cdot d\boldsymbol{l}$ will dominate the RM SF (J. H. Simonetti et al. 1984; A. W. Clegg et al. 1992), as shown in Figure 1. For simplicity, we assume the angular velocity of the FRB source is a constant value ω. In this case, the angle between the LOS and the magnetic field changes as $\Delta\theta = \omega\Delta t$. The value of RM is $\rm RM_0$ at an initial angle θ_0. After some time Δt, the angle between the LOS and the magnetic field changes to $\theta = \theta_0 + \Delta\theta$. One has ${\rm RM_0}\cos(\theta - \theta_0)$. The SF is computed by averaging RM differences across angular scales θ over a range of $0 \leqslant \theta \leqslant \pi$. The geometric contribution to the SF can be written as

$$\begin{aligned} D_g(\Delta\theta) &= \langle [{\rm RM}(\theta) - {\rm RM}(\theta + \Delta\theta)]^2 \rangle \\ &= \frac{1}{2}{\rm RM_0^2}(1 - \cos\Delta\theta). \end{aligned} \quad (10)$$

As shown in the panel (a) of Figure 2, we fit the SF with Equation (10) for $\log(\Delta t) > -2$ days, shown as the red line. The fitting result of average angular velocity is $\omega = 83.388 \pm 3.468\ {\rm rad\ day^{-1}}$, which agrees well with the 1.8 hr orbital period of this binary system. Thanks to the sufficient RM data across multiple periods, the periodic oscillation can be described by Equation (10). The geometric component will show dips at $\omega\Delta t = 2n\pi$, where n is an integer. The first dip occurs at Δt equaling the orbital period P. We also test this speculation using the simulated RM data. The parameters of the binary model to explain the RM variation of FRB 20190520B are used (F. Y. Wang et al. 2022). The orbital period is taken to be 600 days (F. Y. Wang et al. 2022). The simulation lasts for four orbital periods to make the oscillation stage clear. The SF analysis for the simulated data is shown in Figure 3. The fit with Equation (10) is shown as the red line. Because the effect of fluctuations in RM is not included in the simulation, we can see that the SF is completely dominated by the geometric component. The best fit for the period is $P = 605 \pm 3$ days, which is consistent with the period used in the simulation. This result proves that the RM SF in a binary system is dominated by the geometric component if RM variation is caused by the relative orientation of the lines of sight through an ordered magnetic field.

The polarization behavior of some repeating FRBs is similar to PSR B1744–24A (D. Li et al. 2023). For comparison, we also calculate the SF of the RM for FRB 20201124A, which is shown in panel (c) of Figure 2. The SF evolution is similar to that of PSR B1744–24A. They both show a trigonometric-like profile after a steady phase, followed by a decline that can not be interpreted by the turbulence theory. This feature can be well understood by the imprint of the geometric effect. As shown in the panel (c) of Figure 2, we also fit the SF with Equation (10) for $\Delta t > 1$ day, shown as the red line. The derived average angular velocity is $\omega = 0.169 \pm 0.002\ {\rm rad\ day^{-1}}$. It is larger than the angular velocity corresponding to the 80 day orbital period derived from RM variation (F. Y. Wang et al. 2022), i.e., $0.08\ {\rm rad\ day^{-1}}$. The reason is that Equation (10) is only applicable for circular orbit. Moreover, a high eccentric orbit is required to explain the RM variation of FRB 20201124A (F. Y. Wang et al. 2022), and the angular velocity is relatively larger around the pericenter than that in the whole orbital phase.

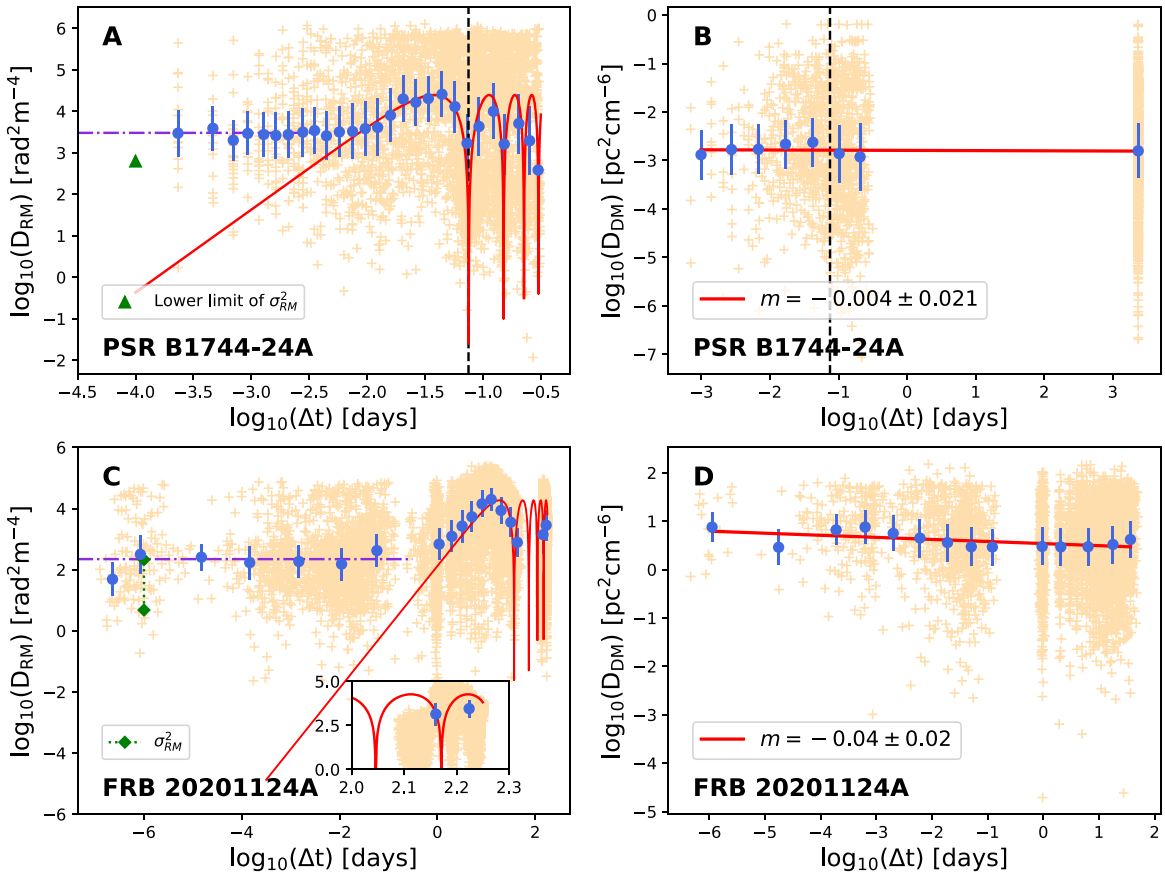

Figure 2. The SFs for PSR B1744–24A and FRB 20201124A. Panel (a): SF of RM for PSR B1744–24A. Orange plus symbols represent the nonbinned data after performing correction, and blue circles indicate binned data with uncertainties estimated as the standard error on the mean. The red solid line is the fit using Equation (10) with $RM_0 = 157 \pm 40$ rad m^{-2}, and the orbital period is ∼1.8 hr. The dot solid line corresponds to the statistical component $D_s = 2927.14$ rad^2 m^{-4}. The black dashed line corresponds to the orbital period of 1.8 hr derived in previous research (D. Li et al. 2023). Panel (b) SF of DM for PSR B1744–24A. The red solid line corresponds to the linear fit with power-law index -0.004 ± 0.021. Panel (c): SF of RM for FRB 20201124A. $RM_0 = 136 \pm 24$ rad m^{-2}, and the orbital period $P = 37 \pm 1$ days. The statistical component is $D_s = 221.88$ rad^2 m^{-4}. Panel (d): SF of DM for FRB 20201124A. The power-law index is -0.04 ± 0.02.

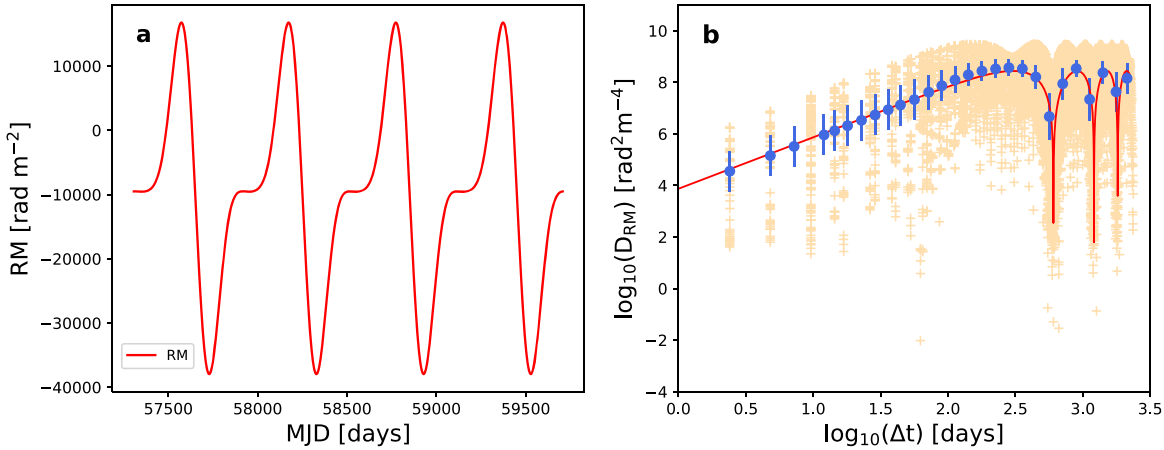

Figure 3. Test of the geometric component using simulations. Panel (a): simulated RM of FRB 20190520B. The red line represents the RM data simulated by the binary model. The model parameters are the same as those used for the observed RM fit (F. Y. Wang et al. 2022). The period is taken as 600 days. Panel (b): SF of simulated RM for FRB 20190520B. Orange plus symbols represent the nonbinned data after doing correction, and blue circles indicate binned data with uncertainties estimated as the standard error on the mean. The red solid line is the fit using Equation (10) with $RM_0 = 16612 \pm 651$ rad m^{-2}, and the orbital period $P = 605 \pm 3$ days, which is consistent the one used in simulations (F. Y. Wang et al. 2022).

Clear evidence of the geometric component has been found from the RM observations in PSR B1744–24A and FRB 20201124A for the first time. The similarity between the SFs of the RM for the two systems gives strong evidence that the source of FRB 20201124A is in a binary system.

We also perform SF analysis for FRB 20180916B, FRB 20190520B, and FRB 20121102A. The results are shown in Figure 4. Similar to those of FRB 20201124A and PSR B1744–24A, the SFs of the RM of three FRBs show a steady phase followed by an increasing phase. Considering the

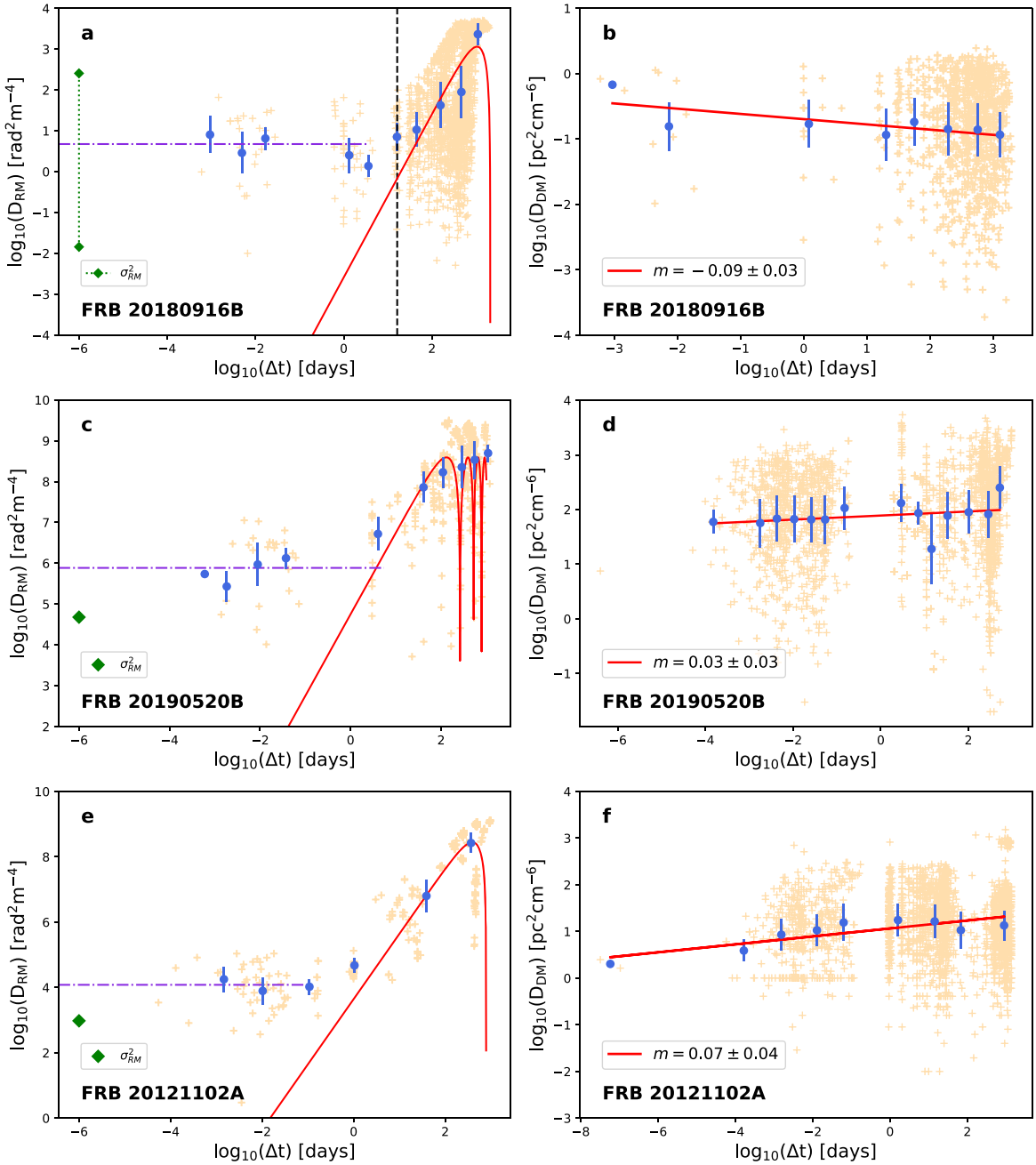

Figure 4. The SFs for FRB 20180916B, FRB 20190520B, and FRB 20121102A. Panel (a): SF of the RM for FRB 20180916B. Orange plus symbols represent the nonbinned data after doing correction, and blue circles indicate binned data with uncertainties estimated as the standard error on the mean. The red solid line is the fit using Equation (10) with $\mathrm{RM}_0 > 33$ rad m^{-2} and the orbital period $P > 2094$ days. The dotted solid line corresponds to the statistic component $D_s = 4.75$ rad^2 m^{-4}. The black dashed line corresponds to the active period of 16.35 days. Panel (b): SF of the DM for FRB 20180916B. The red solid line corresponds to linear fit with power-law index -0.09 ± 0.03. Panel (c): SF of the RM for FRB 20190520B. $\mathrm{RM}_0 > 2 \times 10^4$ rad m^{-2}, orbital period $P > 524$ days, and $D_s = 7.6 \times 10^5$ rad^2 m^{-4}. Panel (d): SF of the DM for FRB 20190520B. The power-law index is 0.03 ± 0.03. Panel (e): SF of the RM for FRB 20121102A. $\mathrm{RM}_0 > 1.7 \times 10^4$ rad m^{-2}, orbital period $P > 785$ days, and $D_s = 1.2 \times 10^4$ rad^2 m^{-4}. Panel (f): SF of the DM for FRB 20121102A. The power-law index -0.07 ± 0.02.

orbital motion in a binary system, we apply Equation (10) to fit the increasing phase. Due to the lack of sufficient observational data and the inflection point shown in SF, the possible periodic oscillation in the RM SF contributed by the geometric component has not been found yet. The fitting results only indicate the lower limits of the orbital period. The potential orbital period could be much longer. Whether these three FRBs are in binary systems still needs to be tested by future observations. The fitting results are summarized in Table 3.

The SFs of the above five sources all show a flat phase for small temporal separation. Below, we discuss its possible physical origin. Except for the geometric component, the statistical component $D_s(\Delta t)$ due to fluctuations in free electron density and magnetic field on timescales smaller than Δt also contributes to the observed SF (J. H. Simonetti et al. 1984; A. W. Clegg et al. 1992). The total SF is

$$D(\Delta t) = D_g(\Delta t) + D_s(\Delta t). \tag{11}$$

If $\mathrm{RM_s}$ is the statistical contribution to the RM from fluctuations on timescales smaller than Δt, then $D_s = 2\langle \mathrm{RM_s^2} \rangle$ (A. W. Clegg et al. 1992). The statistical components of the SF are derived by

Table 3
Fitting Results of SFs

Source	Angular Velocity ω (rad day^{-1})	Orbital Period P (day)	RM_0 (rad m^{-2})	D_s (rad m^{-2})	σ^2_{RM} (rad^2 m^{-2})
PSR B1744–24A	83.388 ± 3.468	0.075 ± 0.002	157 ± 40	2927.14	>625 (D. Li et al. 2023)
FRB 20201124A	0.169 ± 0.002	37 ± 1	136 ± 24	221.88	4.84 ± 213.16 (W.-J. Lu et al. 2023)
FRB 20180916B	<0.003	>2094	>33	4.75	0.01 ± 0.25 (R. Mckinven et al. 2023b)
FRB 20190520B	<0.012	>524	>19,799	761,409.86	47917.21 (Y. Feng et al. 2022)
FRB 20211202A	<0.008	>785	>16,688	12,075.56	954.81 (Y. Feng et al. 2022)
FRB 20190520B (simulated RMs)	0.010 ± 0.001	605 ± 3	16,612 ± 651	...	...

Note. The orbital period is calculated from the average angular velocity. The average angular velocity 83.388 ± 3.468 rad day^{-1} of PSR B1744–24A agrees very well with its 1.8 hr orbital period. The geometric component fitting results of FRB 20180916B, FRB 20190520B, and FRB 20211202A only indicate the lower limits of the potential orbital period and RM_0 due to a small sample of RM data and the absence of a turning feature in their SFs. The simulated RM data for FRB 20190520B are calculated by the binary model.

calculating the mean value of D_s after subtracting the geometric component D_g. The value of D_s varies from 4 to 761,409 rad^2 m^{-4}, as shown in Table 3.

The statistical component of the SF relates to the RM scatter σ_{RM} through $D_s \simeq \sigma^2_{RM}$ (A. W. Clegg et al. 1992). The RM scatter term will cause pulse depolarization through multipath propagation (Y. Feng et al. 2022; F. Y. Wang et al. 2022). Its value can be derived from fitting pulse depolarization. The values of σ^2_{RM} are 4.84–213.16 (W.-J. Lu et al. 2023), 0.01–256 (R. Mckinven et al. 2023b), 47917.21, and 954.81 rad^2 m^{-4} (Y. Feng et al. 2022) for FRB 20201124A, FRB 20180916B, FRB 20190520B, and FRB 20121102A, respectively. Meanwhile, the range of σ^2_{RM} we used here is also considered unlikely for FRB 20180916B (R. Mckinven et al. 2023b). For PSR B1744–24A, the value of the statistical component is 38 rad m^{-2}. From the observed pulse depolarization, the RM scatter (σ_{RM}) is found to be larger than 25 rad m^{-2} (D. Li et al. 2023), which is in the range of the D_s value. From Table 3, the relation $D_s \simeq \sigma^2_{RM}$ is valid for FRB 20201124A, PSR B1744–24A, and FRB 20180916B with sufficient RM observations. The characteristic timescale for σ_{RM} is about $\Delta t \sim 1$ ms. Since RM variation has to occur within the burst duration to cause depolarization, for all sources, the D_s measurements can only be done at $\Delta t > 10^{-6}$ days. For simplicity, a characteristic timescale of $\log(\Delta t) = -6$ days for σ_{RM} has been chosen in Figures 2 and 4. Because the fit of D_s is nearly constant, we extrapolate its value to $\Delta t \sim 1$ ms. The different timescales may cause the discrepancy between D_s and σ_{RM} for FRB 20190520B and FRB 20121102A. Additionally, RM measurements typically encompass measurement errors that are statistically independent or nearly so. As a result, they may also introduce a flat component to the SF at small lags, with a level corresponding to twice the variance of these errors. This effect is coupled with the statistical effect. However, by removing the noise bias when calculating the SFs, the contributions from measurement errors have been eliminated.

We also study the RM SFs for FRB 20180301A, FRB 20220912A, and FRB 20190303A. They are fitted with the power-law function ($D_{RM}(\Delta t) \sim \Delta t^m$). The RM SFs for FRB 20180301A and FRB 20190303A exhibit a power-law form with an index around 0.7, as shown in Figure 5. If we assume the source travels at a constant velocity, i.e., the proper motion of a neutron star, the spatial separation is proportional to the temporal separation. So, the spatial SF has the same behaviors as the temporal SF. The value is consistent with the expectation of the 2D Kolmogorov turbulent medium ($m = 2/3$). FRB 20220912A has small RM values and shows insignificant intraday RM changes with a mean value close to zero (V. Ravi et al. 2023; Y.-K. Zhang et al. 2023). This implies a clean environment around this source. The SF of the RM is presented in Figure 4, which shows an extremely flat SF of the RM. This suggests a nonevolving and uncorrelated RM.

4. Discussion and Conclusions

In this work, SF analysis is used to study the correlations of RM variation for PSR B1744–24A and repeating FRBs. The perfect fit of SF for PSR B1744–24A demonstrates that binary systems should have a geometric component. The SF of the RM for FRB 20201124A has a similar behavior as that of PSR B1744–24A, which suggests it has a binary origin. We have found strong evidence for the geometric component of the SF for the first time. Besides, FRB 20180916B, FRB 20190520B, and FRB 20121102A all have a potential geometric component in the SFs of the RM. The fitting results by the geometric component for these FRBs are shown in Table 3. Due to the limited data, the periodic feature in the geometric component caused by orbital motion has not been observed in these FRBs. So, the fitting results only give a lower limit of the orbital period and RM_0.

The orbital period of FRB 20201124A derived from geometric component fitting is likely to deviate from the true value for several reasons. First, an eccentric orbit is required to explain the steady phase of the RM of FRB 20201124A (F. Y. Wang et al. 2022), and Equation (10) is only applicable for the circular orbit. The uneven sampling intervals of RM observations can lead to the SF being dominated by data from specific orbital phases (e.g., near the pericenter), causing the period inferred from the orbital velocities during these phases to be shorter than the overall orbital period. Second, the evolution of the RM may not be strictly periodic as it is influenced by clumps within the stellar disk (Z. Y. Zhao et al. 2023), which disrupt the ordered magnetic field (A. M. Chen et al. 2019; M. Chernyakova et al. 2021), as well as by interactions between the magnetar and its companion star. Therefore, the RM evolution in the binary system is very likely to be nonperiodic (S. Johnston et al. 1996, 2001, 2005; T. W. Connors et al. 2002; D. Li et al. 2023), making traditional methods for detecting periodicity, such as the Lomb–Scargle method and autocorrelation function, poorly suited for analyzing the RM of FRBs. In contrast, SF analysis is

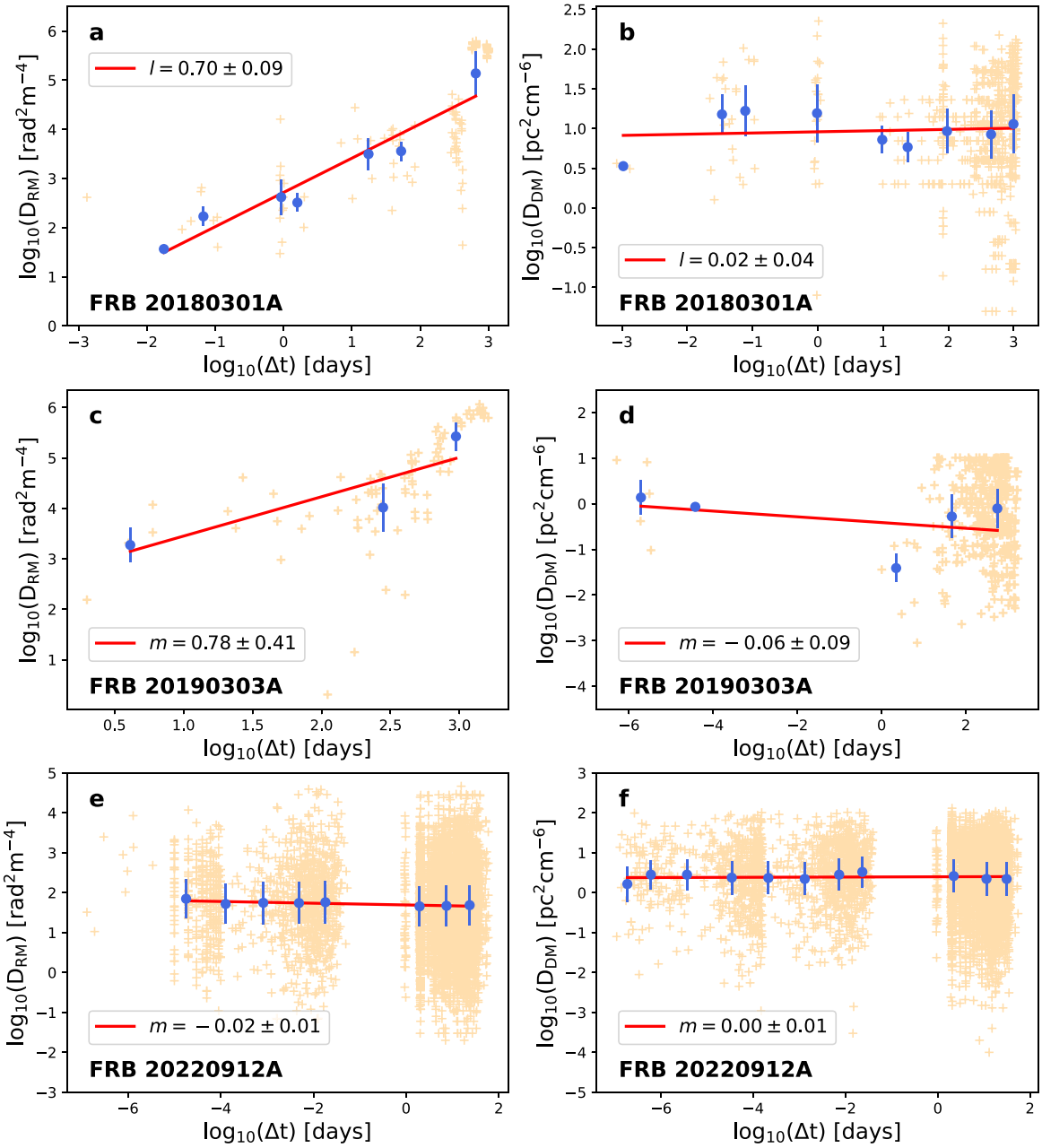

Figure 5. The SFs for FRB 20180301A, FRB 20190303A, and FRB 20220912A. Panel (a): SF of the RM for FRB 20180301A. Orange plus symbols represent the nonbinned data after doing correction, and blue circles indicate binned data with uncertainties estimated as the standard error on the mean. The red solid line corresponds to linear fit with power-law index 0.70 ± 0.09. Panel (b): SF of the DM for FRB 20180301A. The red solid line corresponds to the linear fit with power-law index 0.02 ± 0.04. Panel (c): SF of the RM for FRB 20190303A. The red solid line corresponds to the linear fit with power-law index 0.78 ± 0.41. Panel (d): SF of the DM for FRB 20190303A. The red solid line corresponds to the linear fit with power-law index -0.06 ± 0.09. Panel (e): SF of the RM for FRB 20220912A. The red solid line corresponds to the linear fit with power-law index -0.02 ± 0.01. Panel (f): SF of the DM for FRB 20220912A. The red solid line corresponds to the linear fit with power-law index 0.00 ± 0.01.

effective at identifying potential geometric modulations in the evolution of the RM in FRBs.

In addition to the decline phase and periodic oscillations at larger temporal separations, the geometric component exhibits a power-law rising phase when $\Delta t < 2\pi/\omega$. This behavior resembles the power-law feature of the SF of turbulence under the proper motion assumption. For FRBs that do not show a clear oscillatory phase in their SF (e.g., Figure 4), it is essential to differentiate between the periodic geometric and turbulent components by analyzing their respective power-law indices. Equation (10) can be reformulated in logarithmic space, yielding the first-order expression

$$\log(D_g) = \log(\frac{1}{4}\mathrm{RM}_0^2(\omega\Delta t)^2) = C + 2\log(\Delta t), \quad (12)$$

where C is a constant. The geometric component demonstrates a rising phase with a power-law index of 2, which differs from the expected indices listed in Table 2. However, as previously mentioned, both power-law fitting and geometric fitting are subject to considerable uncertainties due to the limited number of data points. Determining whether these FRBs exhibit

geometric components or a turbulent component will require further investigation in the future.

The power-law indices of RM SFs for FRB 20190303A and FRB 20180301A are weakly sensitive to how the data are binned. The different bins have only a little effect on the results. The range of variation of the power indices m for different methods of binning is relatively small (e.g., $|\Delta m| \lesssim 0.2$). The power-law indices are consistent with the expectation of the 2D Kolmogorov turbulent medium (A. H. Minter & S. R. Spangler 1996).

The SFs of the DM and RM for these FRBs are significantly distinct. The DM SFs for these FRBs are almost unchanging across all temporal separations. The spectral indices for the SF of DMs are from -0.09 to 0.09, which demonstrates that the SF of the DM is independent of temporal separation. The stochastic process may be the intrinsic mechanism driving the DM evolution. This is consistent with the irregular and stochastic evolution of the DM time series of these FRBs. It can be inferred that the changes in the electron density of these FRBs in the observing time are both tiny. Combined with the RM variation, it suggests that the parallel component of the magnetic field is dynamically evolving with time around these FRB sources.

Compared with the complex binary model, which involves many unknown parameters to interpret RM variations, SF analysis has the advantage that the geometric shape of the geometric component is fixed. In our fitting, it is difficult to force fit the observational data through fine-tuning the parameters as there are only two free parameters available to adjust its specific positioning. Therefore, it can give a much more reliable assessment of the binary origin of FRB 20201124A. However, SF analysis heavily depends on the availability of sufficient RM data. For FRBs with limited observational data, the reliability of SF results is significantly lower compared to those derived from FRBs with abundant data (e.g., FRB 20201124A). In the future, monitoring repeating FRBs with radio telescopes will yield larger RM samples, enabling a more reliable diagnosis of their environments and physical origins.

Acknowledgments

We thank the anonymous referee for the helpful comments. We thank Y.P. Yang, Y. Wu, and R. Mckinven for the helpful comments and discussions, Y.Q. Wang for drawing Figure 1, and J.C. Jiang for providing the RM data. This work was supported by the National Natural Science Foundation of China (grant Nos. 12494575 and 12273009), the National SKA Program of China (grant No. 2022SKA0130100), and Postgraduate Research & Practice Innovation Program of Jiangsu Province (KYCX24_0184). This work made use of data from the Five-hundred-meter Aperture Spherical radio Telescope (FAST), a Chinese national mega-science facility built and operated by the National Astronomical Observatories, Chinese Academy of Sciences.

ORCID iDs

Rui-Nan Li https://orcid.org/0009-0007-3326-7827
Zhen-Yin Zhao https://orcid.org/0000-0002-2171-9861
Qin Wu https://orcid.org/0000-0001-6021-5933
Shuang-Xi Yi https://orcid.org/0000-0003-0672-5646
Fa-Yin Wang https://orcid.org/0000-0003-4157-7714

References

Anna-Thomas, R., Connor, L., Dai, S., et al. 2023, Sci, 380, 599
Bandyopadhyay, R., McComas, D. J., Szalay, J. R., et al. 2021, GeoRL, 48, e95006
Bethapudi, S., Spitler, L. G., Li, D. Z., et al. 2024, arXiv:2409.12584
Biskamp, D. 2003, Magnetohydrodynamic Turbulence (Cambridge: Cambridge Univ. Press)
Chawla, P., Andersen, B. C., Bhardwaj, M., et al. 2020, ApJL, 896, L41
Chen, A. M., Takata, J., Yi, S. X., Yu, Y. W., & Cheng, K. S. 2019, A&A, 627, A87
Chernyakova, M., Malyshev, D., van Soelen, B., et al. 2021, Univ, 7, 242
CHIME/FRB Collaboration, Andersen, B. C., Bandura, K., et al. 2019, ApJL, 885, L24
Cho, J., & Lazarian, A. 2002, PhRvL, 88, 245001
Clegg, A. W., Cordes, J. M., Simonetti, J. M., & Kulkarni, S. R. 1992, ApJ, 386, 143
Connors, T. W., Johnston, S., Manchester, R. N., & McConnell, D. 2002, MNRAS, 336, 1201
Cordes, J. M., & Chatterjee, S. 2019, ARA&A, 57, 417
Elmegreen, B. G., & Scalo, J. 2004, ARA&A, 42, 211
Feng, Y., Li, D., Yang, Y.-P., et al. 2022, Sci, 375, 1266
Feng, Y., Li, D., Zhang, Y.-K., et al. 2024, ApJ, 974, 296
Fonseca, E., Andersen, B. C., Bhardwaj, M., et al. 2020, ApJL, 891, L6
Gajjar, V., Siemion, A. P. V., Price, D. C., et al. 2018, ApJ, 863, 2
Gallegos-Garcia, M., Burkhart, B., Rosen, A. L., Naiman, J. P., & Ramirez-Ruiz, E. 2020, ApJL, 899, L30
Gopinath, A., Bassa, C. G., Pleunis, Z., et al. 2024, MNRAS, 527, 9872
Haverkorn, M., Brown, J. C., Gaensler, B. M., & McClure-Griffiths, N. M. 2008, ApJ, 680, 362
Hewitt, D. M., Snelders, M. P., Hessels, J. W. T., et al. 2022, MNRAS, 515, 3577
Higdon, J. C. 1984, ApJ, 285, 109
Hilmarsson, G. H., Michilli, D., Spitler, L. G., et al. 2021a, ApJL, 908, L10
Hilmarsson, G. H., Spitler, L. G., Main, R. A., & Li, D. Z. 2021b, MNRAS, 508, 5354
Jiang, J.-C., Wang, W.-Y., Xu, H., et al. 2022, RAA, 22, 124003
Johnston, S., Ball, L., Wang, N., & Manchester, R. N. 2005, MNRAS, 358, 1069
Johnston, S., Manchester, R. N., Lyne, A. G., et al. 1996, MNRAS, 279, 1026
Johnston, S., Wex, N., Nicastro, L., Manchester, R. N., & Lyne, A. G. 2001, MNRAS, 326, 643
Katz, J. I. 2020, MNRAS: Letters, 501, L76
Kolmogorov, A. 1941, DoSSR, 30, 301
Kumar, P., Luo, R., Price, D. C., et al. 2023, MNRAS, 526, 3652
Lazarian, A., Eyink, G. L., Jafari, A., et al. 2020, PhPl, 27, 012305
Lazarian, A., & Pogosyan, D. 2016, ApJ, 818, 178
Lazarian, A., & Vishniac, E. T. 1999, ApJ, 517, 700
Li, D., Bilous, A., Ransom, S., Main, R., & Yang, Y.-P. 2023, Natur, 618, 484
Li, D., Wang, P., Zhu, W. W., et al. 2021, Natur, 598, 267
Li, R.-N., Zhao, Z.-Y., Gao, Z., & Wang, F.-Y. 2023, ApJL, 956, L2
Lorimer, D. R., Bailes, M., McLaughlin, M. A., Narkevic, D. J., & Crawford, F. 2007, Sci, 318, 777
Lu, W.-J., Zhao, Z.-Y., Wang, F. Y., & Dai, Z. G. 2023, ApJL, 956, L9
Luo, R., Wang, B. J., Men, Y. P., et al. 2020, Natur, 586, 693
Margalit, B., & Metzger, B. D. 2018, ApJL, 868, L4
McKee, C. F., & Ostriker, E. C. 2007, ARA&A, 45, 565
Mckinven, R., Gaensler, B. M., Michilli, D., et al. 2023a, ApJ, 951, 82
Mckinven, R., Gaensler, B. M., Michilli, D., et al. 2023b, ApJ, 950, 12
Michilli, D., Seymour, A., Hessels, J. W. T., et al. 2018, Natur, 553, 182
Minter, A. H., & Spangler, S. R. 1996, ApJ, 458, 194
Montgomery, D., & Turner, L. 1981, PhFl, 24, 825
Ng, C., Pandhi, A., Mckinven, R., et al. 2024, arXiv:2411.09045
Niu, C. H., Aggarwal, K., Li, D., et al. 2022, Natur, 606, 873
Piro, A. L. 2016, ApJL, 824, L32
Piro, A. L., & Gaensler, B. M. 2018, ApJ, 861, 150
Pleunis, Z., Good, D. C., Kaspi, V. M., et al. 2021, ApJ, 923, 1
Rajwade, K. M., & van den Eijnden, J. 2023, A&A, 673, A136
Ravi, V., Catha, M., Chen, G., et al. 2023, ApJL, 949, L3
Ryu, D., Kang, H., Cho, J., & Das, S. 2008, Sci, 320, 909
Saha, P., Bharadwaj, S., Roy, N., Choudhuri, S., & Chattopadhyay, D. 2019, MNRAS, 489, 5866
Shaikh, D., & Zank, G. P. 2010, JPlPh, 76, 183
Shimoda, J., Akahori, T., Lazarian, A., Inoue, T., & Fujita, Y. 2018, MNRAS, 480, 2200
Simonetti, J. H., & Cordes, J. M. 1986, ApJ, 310, 160

Simonetti, J. H., Cordes, J. M., & Spangler, S. R. 1984, ApJ, 284, 126
Spitler, L. G., Scholz, P., Hessels, J. W. T., et al. 2016, Natur, 531, 202
Wang, F. Y., Zhang, G. Q., Dai, Z. G., & Cheng, K. S. 2022, NatCo, 13, 4382
Wang, R., Wang, S., Lu, Q., et al. 2023, NatAs, 7, 18
Wu, Q., & Wang, F.-Y. 2024, ChPhL, 41, 119801
Xu, H., Niu, J. R., Chen, P., et al. 2022, Natur, 609, 685
Xu, S., Weinberg, D. H., & Zhang, B. 2021, ApJL, 922, L31
Xu, S., & Zhang, B. 2016, ApJ, 824, 113
Xu, S., & Zhang, B. 2020, ApJL, 898, L48
Xu, S. B., Huang, S. Y., Sahraoui, F., et al. 2023, GeoRL, 50, e2023GL105463
Yang, Y.-H., & Dai, Z.-G. 2019, ApJ, 885, 149
Yang, Y.-P., Xu, S., & Zhang, B. 2023, MNRAS, 520, 2039
Yang, Y.-P., & Zhang, B. 2017, ApJ, 847, 22
Zhang, B. 2018, ApJL, 854, L21
Zhang, B. 2023, RvMP., 95, 035005
Zhang, B., & Yan, H. 2011, ApJ, 726, 90
Zhang, Y.-K., Li, D., Zhang, B., et al. 2023, ApJ, 955, 142
Zhao, Z. Y., Chen, K., Wang, F. Y., & Dai, Z.-G. 2024, MNRAS, 530, 1644
Zhao, Z. Y., & Wang, F. Y. 2021, ApJL, 923, L17
Zhao, Z. Y., Zhang, G. Q., Wang, F. Y., & Dai, Z. G. 2023, ApJ, 942, 102
Zhao, Z. Y., Zhang, G. Q., Wang, Y. Y., Tu, Z.-L., & Wang, F. Y. 2021, ApJ, 907, 111